Non-triggering and then triggering of a repeating aftershock sequence in the Dead Sea by the 2023 Kahramanmaraş earthquake pair: Implications for the physics of remote delayed aftershocks

A. Inbal, Department of Geophysics, Tel Aviv University, Tel Aviv, Israel

A. Ziv, Department of Geophysics, Tel Aviv University, Tel Aviv, Israel

I. Lior, Institute of Earth Sciences, The Hebrew University, Jerusalem, Israel

R.N. Nof, Geological Survey of Israel, Jerusalem, Israel
A. S. Eisermann, Department of Geophysics, Tel Aviv University, Tel Aviv,

Israel

1. Abstract

Most aftershocks occur in areas experiencing large co-seismic stress changes, yet some occur long after the mainshock in remote lightly-stressed regions. The triggering mechanism of these remote delayed aftershocks is not well understood. Here, we study aftershocks occurring in the Dead Sea (DS) area following the 2023 M_w7.8 and M_w7.6 Kahramanmaraş earthquakes. Most aftershocks cluster along previously quiescent structures off- the main the DS fault strand. Visual inspection disclosed three aftershocks instantaneously triggered by the M_w7.6 in the northern DS basin, and match-filtering revealed a delayed aftershock. Waveform similarity and temporal clustering suggest the northern DS aftershocks re-rupture a stick-slip patch loaded by surrounding creep. Velocity-gradient seismograms show the M_w7.6 exerted larger transient stresses than the M_w7.8, which may explain triggering by the Mw7.6, but not by the Mw7.8. This account of

instantaneously-triggered repeaters underscores the role of interactions between aseismic and seismic slip in remote triggering.

2. Introduction

Aftershocks play an important role in the relaxation and redistribution of stress perturbations caused by major earthquakes [*Ben-Zion et al.*, 2003; *Ziv and Schmittbuhl*, 2003]. While the vast majority of them occur long after the passage of the seismic waves, a tiny fraction may occur during the surface-wave train [*Hill et al.*, 1993; *Brodsky et al.*, 2000]. From a physical standpoint, it is useful to categorize aftershocks according to their time of occurrence with respect to the passage of the seismic waves excited by the mainshock source. Here, aftershocks that occurred during the wave–induced ground shaking are referred to as instantaneous aftershocks, and those that occurred afterward are referred to as delayed aftershocks. It is well established that the majority of the delayed aftershocks occur in places where the static (i.e., permanent) stress changed in a manner that encourages fault slip [*King et al.*, 1994]. Yet, some of them occur in remote sites, where the stress changes caused by the mainshock are tiny [*Gomberg et al.*, 2001; *Kilb et al.*, 2000]. The physical mechanism that gives rise to remote delayed aftershocks is not well understood. Furthermore, not all delayed aftershocks are caused directly by the stress change imparted by the mainshock. Instead, a notable fraction of them is induced by multiple stress transfers from early aftershocks to the site of subsequent ones [*Helmstetter et al.*, 2003; *Marsan*, 2005; *Ziv*, 2006a, b], or by remotely triggered fault creep [*Inbal et al.*, 2017]. Aftershocks of aftershocks and triggered creep may occur in areas where the stress perturbation (positive or negative) induced by the mainshock is small, and may thus explain the occurrence of some delayed aftershocks in remote sites [*Ziv*, 2006a, b; *Inbal et al.*, 2017].

The 2023 M_w7.8 and M_w7.6 Kahramanmaraş earthquake pair from Eastern Turkey, caused a dramatic earthquake rate increase over vast areas (Figure 1a). This activity was very well recorded by strong-motion sensors located along the northern Dead Sea (DS) basin, which are part of the dense Israel Seismic Network (ISN) for earthquake early warning - the TRUAA network (Kurzon et al., 2020). In this study we examine a sequence of four repeating aftershocks in the northern DS basin, three of which are instantaneous aftershocks in the sense that they occurred during the passage of the surface waves of the M_w7.6 earthquake (Figure 1b). The importance of this finding is twofold. First, the triggering of aftershocks on a portion of the Dead Sea Transform (DST) that has not ruptured in recent history, suggests that rupture of that segment may have been promoted by the Kahramanmaraş earthquakes. Second, the observations shed new light on the triggering mechanism of remote aftershocks.

3. The remotely triggered Dead Sea aftershock sequence

3.1. Remote delayed aftershocks throughout Palestine and Israel

The DST, which accommodates 4-5 mm/yr left-lateral motion between the Sinai sub-plate and the Arabian plate (Figure 1a), is the most active fault affecting the study area. Yet, the most intense earthquake rate change due to the 2023 Kahramanmaraş earthquakes occurred off the main DST strand. For example, just south of the Palestinian city of Nablus, the earthquake rate has surged by more than two orders of magnitude (Figure 1a). Up to the time interval reported here, fault slip-rates in that region were reported to be below 0.5 mm/year, and thus these faults were considered to be seismically inactive [*Sharon et al.*, 2020]. Another area of notable aftershock activity is located in the Mediterranean Sea, offshore Haifa (Figure 1a). This activity is likely associated with the seaward extension of the extensional Carmel Fault, or with the southern extension of the Mount Lebanon Thrust. Two other notable but spatially-limited

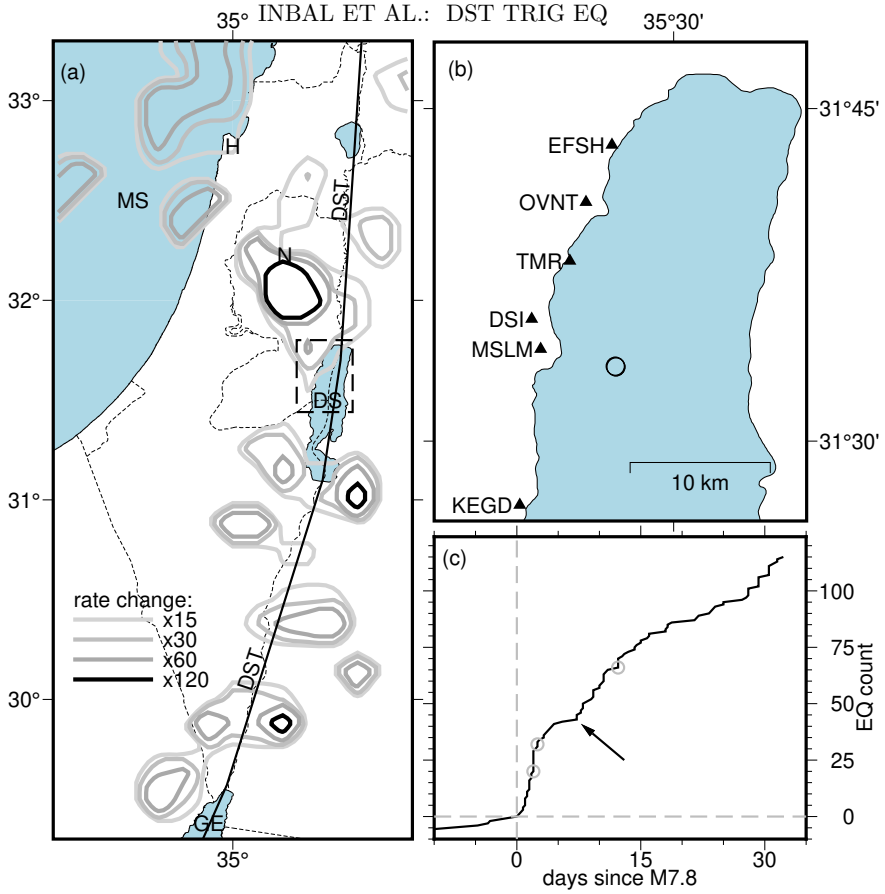

Figure 1: Study area location maps and earthquake count. (a) A map of aftershock rate change, calculated for a sliding window of 0.25 by 0.25 degrees, using: $(N_{as}/T_{as})/(N_{bg}/T_{bg})$, where "$as$" and "$bg$" stand for aftershock and background intervals, respectively, N signifies earthquake count, T signifies the interval, and T_{as} and T_{bg} are equal to 32 days and 10 years, respectively. The dashed square indicates the location of the map shown in panel b, dashed line signifies political borders, and solid line marks the location of the DST. DST, Dead Sea Transform, DS, Dead Sea; MS, Mediterranean Sea; GE, Gulf of Eilat; N, Nablus; and H, Haifa. (b) A map showing the epicenters of the 4 repeating aftershocks (circles), and the TRUAA's strong-motion stations in that area (triangles). (c) Study area earthquakes count as a function of time with respect to the time of the 2023 M_w7.8 earthquake. The circles mark the three local aftershocks with M>3.3, and the arrow marks a point of notable aftershock rate increase.

rate increases are resolved east of the southern DS basin and northeast of the Gulf of Eilat. In contrast, the northern DS basin, which is a major pull-apart basin located along the DST, has experienced only a modest earthquake rate increase. In light of these observations, we infer that

the pre-stress levels on the structures on either side of the main DST strand are presently higher than on the DST system itself. The implications of this result for earthquake risk assessment, and the development of earthquake mitigation strategies are far-reaching and warrant further consideration.

A plot of cumulative earthquake count as a function of time discloses complex temporal clustering, with large variations in the rate of earthquake occurrence (Figure 1c). Some of the jumps in the earthquake rate are attributable to local $M > 3.3$ aftershocks that act locally as mainshocks of small aftershock sequences (marked by empty circles on Figure 1c), whereas others, but most notably the one marked by an arrow, can neither be associated with local mainshocks, nor with regional ones. That notable increase is mostly attributable to a seismic swarm located to the south of Nablus. Given the timing relative to the Kahramanmaraş earthquakes, the pervasive lack of instantaneous triggering, and the lack of notable local mainshocks, it is likely that additional mechanisms triggered the seismicity showing up as unexplainable steps in the cumulative earthquake count versus time diagram. One possibility is the Kahramanmaraş earthquake pair triggered aseismic fault slip, which may be detectable geodetically.

3.2. Discerning instantaneous aftershocks

In search of local earthquakes within the surface and coda waves of the Kahramanmaraş mainshocks, we scanned all the ISN recorded strong-motion and broad-band seismograms of the M_w7.8 and M_w7.6 earthquakes. By band-pass filtering the seismograms between 8 and 16 Hz, we identified 3 microearthquakes that occurred during passage of surface waves excited by the M_w7.6 (Figure 2a). These are best observed in the strong-motion seismograms recorded by the MSLM and DSI stations, and to a lesser extent also by TMR, OVNT, EFSH, and KEGD. The P- and S-phase arrivals of the earliest aftershock to MSLM are well resolved (Figure 2b, 2c, and S2),

and constrain its hypocentral distance to about 16 kilometers. Low-pass filtered ground velocity (integrated accelerations) time-series at station MSLM are shown in Figure 2a. Inspection of these, as well as other, low-pass filtered accelerograms indicate that the strongest ground motion in the DS area is measured on the transverse component, which is associated with Love wave propagation. A detailed analysis of the surface-wave induced strain in the northern DS area is presented in Section 6.1.

3.3. Supplementing the Dead Sea aftershock catalog using Match Filter Analysis

To identify multiplets of event #1 (registered or not in the GSI catalog), we implemented the template-based Match Filter Analysis (MFA ; *Gibbons and Ringdal* [2006]). We extracted a three-component template waveform, consisting of a portion of the P-wave train excited by event #1. The template duration is 1.8 s, starting from 0.3 s prior to the P-wave arrival at the four nearest stations (in Figure 1b), and filtered between 8 to 16 Hz. The MFA detection process operates as follows: First, we correlate the template waveform across a 2.13 year-long time-series (segmented into days) starting from January 1, 2021, and ending on February 21, 2023, with 90% overlap between adjacent temporal windows. Next, we correlate the correlations of the vertical channels carrying the template across stations, thus deriving the inter-station time offsets corresponding to the template. Finally, we shift the template cross-time three-component correlations according to the cross-station offsets, and stack the cross-correlations. These were scanned for multiplets. For a positive hit, we require the value of this function to exceed its 1-hour median by 9 times the Median Absolute Deviation of that hour. We turn each successful hit into a template, and repeat the same procedure as for event #1.

Analysis of the 9 hour interval between the M_w7.8 and M_w7.6 mainshocks did not yield any positive detections, and the analysis of the 17 days following the M_w7.6 earthquake yielded 3 hits.

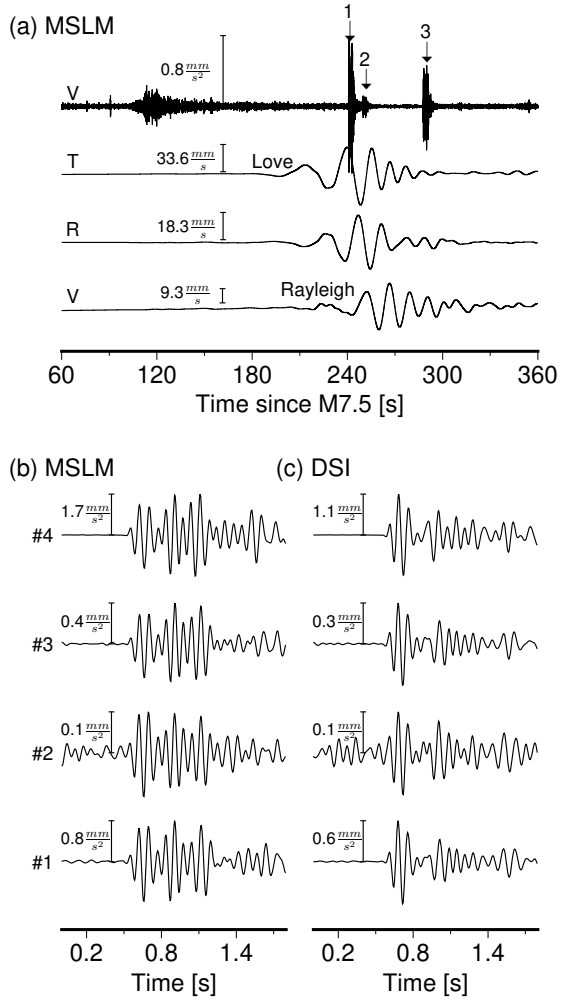

Figure 2: Ground acceleration and velocity recorded at stations MSLM and DSI showing the surface wave arrivals, the instantaneously triggered earthquake and the first two aftershocks. V, T, and R are for the vertical, transverse, and radial component of motion, respectively. The numbers refer to the events listed in Table 1. (a) Band- and low-pass filtered seismograms from MSLM. Top trace is band-pass filtered between 8 to 16 Hz, and the three bottom traces are low-pass filtered above 0.1 Hz. Time is referenced to the M_w7.6 origin time. Arrows show arrivals due to events #1 to #3. (b,c) Vertical accelerograms containing the P-wave train of the 4 earthquakes of the northern DS basin repeating aftershock. The traces are filtered between 8 to 16 Hz and aligned on the P-wave arrival. The vertical bars are for scale. Event #1 was instantaneously triggered during the passage of surface waves excited by the February 6, 2023 M_w7.6 Kahramanmaraş earthquake. Left panel: Station MSLM. Right panel: Station DSI.

We did not detect similar events occurring in the two years before the M_w7.8. The newly detected earthquake source parameters are listed in Table 1 (Supplementary Materials), and their P-wave seismograms are shown in Figure 2. They exhibit great similarity to the instantaneously triggered earthquake template (event #1), especially at station MSLM, located a few km from event #1 epicenter (Figure 2). Between February 6 to February 17, 2023, the ISN located 6 earthquakes occurring within 15 km of event #1, one of them passed our detection criteria (event #4, see Table 1). Based on waveform similarity, we suggest that the 4 aftershocks re-ruptured an isolated fault patch. The MFA further indicates that this patch was previously inactive for at least two years.

4. Master event location

The four hypocenters were located in two steps. In the first, we implemented a grid-search approach, and used the 1-D velocity model of *Gitterman et al.* [2003]. In the second step, we used the master event location approach to get relative locations [*Fitch*, 1975]. We chose the latest earthquake (event #4) as a master event, as its initial location was most tightly constrained. High waveform similarity allowed us to improved the P-phase picking of the 3 slave events by cross-correlation master event P-wave arrivals. Furthermore, we fixed the depths of the slave events, to that of the master. The result of the master-slave event locations (Figure 1b) indicates the four ruptures overlap, supporting the view of repeating aftershocks.

5. Temporal variations

5.1. Recurrence times

The spatial clustering of the four earthquakes, and their strong waveform similarity are consistent with the possibility that this series resulted from repeated slip events on an isolated

stick-slip patch that is embedded within an otherwise aseismic fault [*Vidale et al.*, 1994; *Nadeau et al.*, 1994; *Marone et al.*, 1995]. The effect of perturbing the stress of such a configuration is to increase the creep rate on the aseismic segment. If the slip on that segment is resisted by a logarithmic rate- strengthening friction, the rate of creep is expected to decay as $1/t$ following a stress step, with t being the elapsed time since the stress perturbation [*Schaff et al.*, 1998; *Chen and Lapusta*, 2009]. Consequently, the stressing rate on the stick-slip patch varies with the reciprocal of time, and the following relation between the recurrence time, τ, and t is predicted [*Schaff et al.*, 1998]:

$$\frac{1}{\tau_i} = \frac{a}{t_i}, \tag{1}$$

where a is an empirically determined fitting coefficient, and i is the earthquake index. The right-hand side of (1) is similar to that of the well-known Omori law [*Omori*, 1894], which provides good fit to the vast majority of aftershock sequences observed following major earthquakes. In contrast to the Omori law, this function is equated here to the reciprocal of the recurrence time, which may be thought of as the instantaneous rate of earthquake occurrence. If instead, the creep is resisted by viscous stresses (with friction being linearly proportional to slip rate), the rate of creep is expected to decay exponentially [*Segall*, 2010], and so is the instantaneous earthquake rate:

$$\frac{1}{\tau_i} = a \exp(-bt), \tag{2}$$

with b being another fitting coefficient. Relations (1) and (2), hereafter refer to as the Omori and Exponential models, respectively, provide means for corroborating the isolated stick-slip patch model, and discriminating between the two friction models. The reciprocal of the repeating quakes recurrence time as a function of time since the first aftershock is shown in Figures 3a on a log-log space. Because the number of data is small, it is not evident which relation best fits the

recurrence intervals. To quantify the degree to which the temporal evolution of this earthquake cluster is more consistent with relation (1) than (2), an Omori-versus-Exponential Fitting Index (FI) is introduced:

$$FI = \frac{L^2_{\mathrm{Exp}} - L^2_{\mathrm{Omori}}}{L^2_{\mathrm{Exp}} + L^2_{\mathrm{Omori}}}, \tag{3}$$

where L^2_{Omori} and L^2_{Exp} are the norm-2 misfits to equations 1 and 2, respectively. This function may range between -1 and +1, with FI=-1 if the $1/\tau$ time-series is perfectly modeled by the exponential relation in (2) , and FI=1 if it is perfectly modeled by the Omori function in (1). The fitting index of the time-series in question is equal to 0.8, thus strongly suggesting that the data are better fit with (1) than with (2). Yet, given the small dataset, it is important to assess the extent to which this result is statistically meaningful. In the supplementary materials we present the result of a Monte Carlo testing, showing that the possibility of FI=0.8 emerging by chance may be rejected at greater than 96% confidence level.

5.2. Relative seismic moments

We assume the earthquake spectra follow the well-known ω^2 model [*Aki*, 1967; *Brune*, 1970], and recover the source properties directly from the observed spectral amplitudes. The low-frequency displacement spectral plateau Ω_0 and the seismic moment are related as [*Aki and Richards*, 2002]:

$$M_0 = \Omega_0 RC, \tag{4}$$

where R is the hypocentral distance and collects site and path parameters and the radiation pattern. Note that the seismic moment estimates are insensitive to the decay rate at frequencies well-above the source' characteristic frequency. The low-frequency spectral plateau, Ω_0 , may be computed in the frequency or time domain. Here, Ω_0 is estimated using the simple time-domain

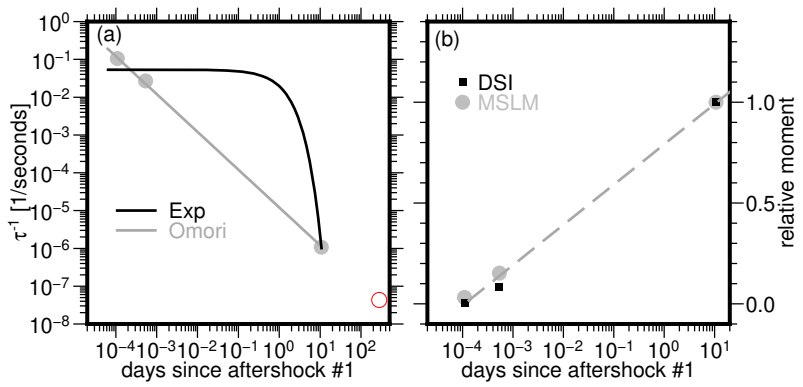

Figure 3: Summary of temporal analysis. (a) Log-log diagram of the reciprocal of recurrence time as a function of time since the first aftershock. (b) Relative moment as a function of recurrence time for events 2-4, calculated separately for accelerograms recorded at stations MSLM (gray circles) and DSI (black squares). Red symbols correspond to the $N+1$ predictions.

expression of *Lior and Ziv* [2020]:

$$\Omega_0 = 2\sqrt{T} D_{rms}^{1.5} / V_{rms}^{0.5}, \tag{5}$$

where T is the data interval, and D_{rms} and V_{rms} are the displacement and velocity root-mean-squares (rms), respectively. The above expression is valid in the far-field, and does not require prior knowledge of the source corner frequency and attenuation effects. For these reasons, use of this time-domain expression is most advantageous for small earthquakes and/or data of limited frequency band-width [*Lior and Ziv*, 2020]. Because repeating earthquakes recorded at a given station share the same site and path parameters, the seismic moment of earthquake j relative to that of earthquake k, calculated using seismograms recorded by station i may expressed as:

$$\frac{M_0^{ij}}{M_0^{ik}} = \frac{(D_{rms}^{1.5}/V_{rms}^{0.5})_{ij}}{(D_{rms}^{1.5}/V_{rms}^{0.5})_{ik}}. \tag{6}$$

177 We calculated relative seismic moments from doubly-integrated accelerations at MSLM and
178 DSI using 4 seconds-long intervals starting at the S-phase onset. Because events 1 to 3 coincide
179 with the passage of the surface waves of the M_w7.6 Kahramanmaraş earthquake, they may only be
180 studied in a limited frequency band. Therefore, a 6-18 Hz bandpass filter was applied following
181 each integration. The relative seismic moments exhibit a 20% steady increase of the relative
182 moment per 10-fold increase time elapsed since event 4. (Figure 3b). This trend is consistent
183 with experiments showing that friction increases with the logarithm of time since the previous
184 slip episode [*Dieterich*, 1972; *Scholz et al.*, 1972; *Scholz and Engelder*, 1976].

6. Discussion

185 The DS repeating aftershock sequence reported in this study differs from previously reported
186 ones in two main respects. First, while previous repeaters were located in the near-field of the
187 mainshock the DS sequence is clearly located at its far-field. Second, the triggering mainshock
188 occurred just 9 hours after a larger mainshock that did not trigger instantaneous aftershocks
189 in the study area or delayed aftershocks near the DS sequence. These differences create an
190 opportunity for revisiting previous paradigms, and introducing new ones.

6.1. Triggering mechanism for delayed remote aftershocks

191 It is difficult to explain the triggering of remote delayed aftershocks by means of stress trans-
192 fer because of the small permanent stress changes. In contrast, explaining the occurrence of
193 instantaneous aftershocks is more straightforward because their magnitude seems sufficient for
194 triggering of critically-stressed faults [*Gomberg and Johnson*, 2005]. Thus, if instantaneous trig-
195 gering was a common phenomena, one could have imagined a stress transfer process, whereby
196 delayed aftershocks are triggered by the instantaneous aftershocks that act locally as small main-

shocks [*Helmstetter et al.*, 2003; *Ziv*, 2006a; *Heimisson*, 2019]. Because, however, our search for instantaneous triggering yielded only 3 co-located aftershocks within the northern DS basin, this triggering mechanism cannot explain the widespread delayed aftershocks reported in this study (Figure 1a). Here we suggest that the observations presented in this study shed new light on the triggering mechanism of remote aftershocks.

It is a widely held notion that the re-rupturing of a given fault patch, with recurrence intervals that decay as the reciprocal of elapsed time since the first aftershock, requires strong interaction with a velocity-strengthening creeping segment [*Schaff et al.*, 1998]. As this sequence occurred in the far-field of its trigger, and in an area that did not experience any earthquake rate increase prior to its onset, we can further infer that remote delayed aftershocks result from the stress change induced by local creep. That creep triggered by seismic waves excited by the mainshock. Once in motion, they stress their surroundings, and trigger instantaneous or delayed aftershocks. Indeed, the sequence documented in this study consists of four aftershocks, of which the first three are instantaneous, and the fourth is delayed. The interaction between aseismic and seismic slip is rather complex. The stick-slip patch is being stressed by the surrounding creep during inter-event intervals, and is stressing it with each slip episode. Thus, deeper understanding of this process may require forward modeling.

6.2. Implications of the non-triggering by the M_w7.8 earthquake

That the repeating aftershock sequence was triggered instantaneously by a M_w7.6 earthquake just 9 hours after an equally distant M_w7.8 earthquake raises the question as to what may be learned from the non-triggering of that sequence by the largest of the two. The non-triggering by the M_w7.8 and the triggering by the M_w7.6 earthquakes just 9 hours later may be understood if the transient stress change induced by the latter was notably larger than that induced by the

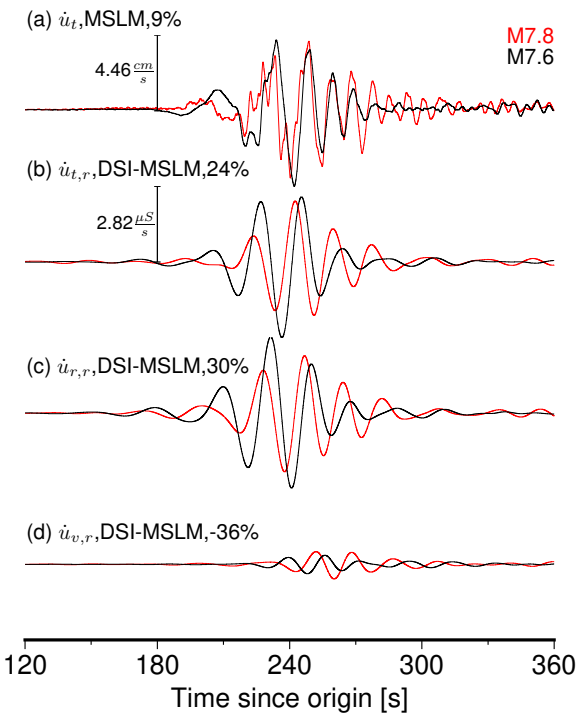

Figure 4: Ground velocity and its spatial gradient as a function of time. $\dot{u}_t$ denotes the transverse component of velocity. $\dot{u}_{t,r}$, $\dot{u}_{r,r}$, and $\dot{u}_{v,r}$ are for gradients of the transverse, radial, and vertical velocity components computed along the radial direction, respectively. Number in percentage denotes the difference between the maximum M_w7.6 and M_w7.8 gradient maxima relative to the maximum amplitude of the M_w7.8 for each component (i.e. positive is for increase in the M_w7.6 maxima gradient amplitude). a. Station DSI low-pass filtered above 1 Hz. b-d. The velocity gradient computed using differences between DSI and MSLM (see Figure 1 for station locations). Seismograms were band-pass filtered between 32 to 16 s before differentiation. Units are in micro-strain/s.

former. Indeed the Peak-Ground-Velocity (PGV) induced by the M_w7.6 in the DS area is by about 10% larger than that induced by the M_w7.8. Equating the peak strain to the product between the PGV and the slowness [e.g *Benioff*, 1935; *Mikumo and Aki*, 1964] yields an equally larger strain - and therefore also stress change - for the M_w7.6 than for the M_w7.8. It is difficult to attribute the notably different triggering effect of the two earthquakes to a 10% difference in the stress perturbations at the same site.

Gomberg and Agnew [1996] reported large discrepancies between strain calculation using the above approach and direct strain-meter measurements. Thus, to address the question as to what may be learned from the non-triggering by the M_w7.8, it is instructive to obtain a more direct strain measurement. Since strain-meters are not available in the study area, we implement an alternative approach that takes advantage of the network's alignment being sub-parallel to the radial direction pointing from the northern DS basin to the M_w7.6 source. By taking the difference between the same-component long-period (>10 s) velocity time-series measurements at two nearly radially-aligned stations, and dividing them by the inter-station distance projected onto the radial direction, we obtained timelines of the following velocity gradients: $\dot{u}_{r,r}$, $\dot{u}_{t,r}$, and $\dot{u}_{v,r}$, where t, r, and v represent the transverse, radial, and vertical components, respectively. In doing so, we require that the inter-station distances be less than about a quarter of the seismic wave-length (after filtering). The main advantage of this approach with respect to the one described above is that it does not rest on the assumption that the slowness between each station pair equals the slowness measured across the network. Under the assumption that the waves can be treated as perfectly planar, the strain rate tensor components can be approximated from the measured gradients [*Gomberg and Agnew*, 1996]. In this case $\dot{\varepsilon}_{rr} \approx \dot{u}_{r,r}$, $\dot{\varepsilon}_{tr} \approx 1/2\dot{u}_{t,r}$, and $\dot{\varepsilon}_{vr} \approx 1/2\dot{u}_{v,r}$, where $\dot{\varepsilon}_{rr}$ and $\dot{\varepsilon}_{tr}$ are the horizontal dilatational and shear strains, respectively, and $\dot{\varepsilon}_{vr}$ is the shear strain acting on vertical planes parallel to radial direction.

The results of our new approach for deformation rate analysis are presented in Figure 4 for the two nearest stations to the DS aftershock sequence - MSLM and DSI. We find that the differences between M_w7.8 and the M_w7.6 are more notable in the deformation rate domain than they are in the raw velocity time-series. Comparing the M_w7.8 and the M_w7.6 deformation rate time-series, we find that the most notable positive gradient increases are observed on the transverse

and radial components, whereas the peak M_w7.6 vertical component gradient is reduced relative to the M_w7.8. The peak dynamic long-period (>10 s) transverse velocity gradient due to the M_w7.6 is about 30% larger than the M_w7.8 peak gradient, however individual phases that differ by up to a factor of two appear after differentiation (Figure 4b). We examined the deformation rate gradients using all neighboring station pairs along the western shore of the DS lake (Figure 1a). This indicated that M_w7.6 transient shear strain is increased by 30% to 40% relative to the M_w7.8 at all the northern DS basin station pairs, that dilatational strain peak for MSLM-DSI increased by 30% but was reduced at the adjacent station pairs, and that the M_w7.6 transient shear stress peaks halfway between MSLM and DSI, in agreement with the repeater location.

Two source-related effects may combine to produce 10% stronger ground shaking and 30% to 40% strain rate for the M_w7.6 than for the M_w7.8. The first factor, affecting mainly the long-period strain rates, is the azimuthal dependence of the Love wave radiation pattern. The M_w7.6 fault strikes approximately east-west, and is thus well oriented with respect to the Love-wave radiation towards the DS, while the M_w7.8 strikes approximately north-north-east, thus producing minimum Love-wave radiation in that direction. This eastward strike rotation is sufficient in order to offset the level of seismic energy radiated from the M_w7.6 source to an amplitude comparable to the one radiated by the M_w7.8 source. A second factor, affecting mostly the short-period ground shaking between the two mainshocks is their static stress drops. The M_w7.8 ruptured a relatively large fault area of about 1400 km^2 that slipped on average by about 5 m, whereas the M_w7.6 ruptured about half the M_w7.8 fault area, and its average slip is about 2.5 m [*Barbot et al.*, 2023]. Since the stress drop is proportional to the ratio between the average slip and the fault length, those differences decreased the M_w7.8 stress drop by a factor of about 3 relative to the M_w7.6 stress drop. We suggest that the larger stress drop and

271 the favorable orientation increased the M_w7.6 S-wave (and hence Love-wave) energy radiation,
272 explaining the instantaneous triggering by that earthquake.

7. Conclusive remarks

273 The 2023 Kahramanmaraş earthquake pair triggered widespread aftershock activity throughout
274 Palestine and Israel. Surprisingly, the strongest earthquake rate increase is observed on either side
275 of the DST and in the Mediterranean Sea offshore Haifa, suggesting that secondary structures in
276 the study area are presently more prestressed than the DST main strand. Earthquake count as a
277 function of time reveals complex evolution, with activity bursts that are attributable to $M_w > 3$,
278 which act as local mainshocks. Other seismicity rate jumps that cannot be explained by local
279 triggering, may be indicative of aseismic deformations.

280 Visual inspection of high-pass filtered accelerograms of the M_w7.8 and M_w7.6 Kahramanmaraş
281 earthquakes discloses three instantaneously triggered aftershocks of the latter in the northern
282 DS basin. A delayed aftershock is revealed via MFA. Based on strong waveform similarity and
283 co-location, with location uncertainties that are smaller than the estimated rupture dimensions,
284 it is inferred that the four aftershocks correspond to a sequence of repeaters. Temporal analyses
285 are presented, which indicate that the logarithm of repeat time and the seismic moment increase
286 linearly with the logarithm of elapsed time since the first aftershock.

287 This first account of an instantaneously triggered repeating aftershock sequence at the far-
288 field of its trigger underscores the role of the interaction between aseismic and seismic slip in
289 remote aftershock triggering [*Inbal et al.*, 2017]. A comparison between peak ground shaking
290 and spatial derivative of velocity seismograms of the two Kahramanmaraş earthquakes suggests
291 larger transient stress change in the DS during the M_w7.6 than during the M_w7.8. This may

explain why the DS aftershocks were triggered by the M_w7.6, but not the M_w7.8, despite the latter preceding the former by just a few hours.

Finally, given a sequence of $N \geq 3$ aftershocks, with a τ versus t relation obeying Equation 1, the timing of the $N+1$ aftershock may be predicted using: $t_{i+1} = t_i \frac{a}{a-1}$. Thus, should the current $1/\tau$ trend continue, the next aftershock is expected to occur about 278 days after the mainshock (using a=1.04 and t_4=10.72 days, see red open circle in Figure 3a). Furthermore, from the relative moment versus time plot in Figure 3b, the size of that earthquake is expected to be 20% larger than that of the largest aftershock. These predictions may require some revision in case that the local stress field would be altered by some external source, such as a local or regional earthquake, or a slow slip episode on a nearby segment.

Acknowledgments.

Open Research. Data from the IS network are available at https://doi.org/10.5281/zenodo.7980346. The seismic catalog is available at https://seis.gsi.gov.il/fdsnws/event/.

References

Aki, K. (1967), Scaling law of seismic spectrum, *J. Geophys. Res.*, *72*(4), 1217–1231, doi: https://doi.org/10.1029/JZ072i004p01217.

Aki, K., and P. Richards (2002), *Quantitative Seismology*, second ed., Univ Science Books, doi: 10.1016/S0065-230X(09)04001-9.

Barbot, S., H. Luo, T. Wang, Y. Hamiel, O. Piatibratova, M. T. Javed, C. Braitenberg, and G. Gurbuz (2023), Slip distribution of the February 6, 2023 Mw 7.8 and Mw 7.6, Kahramanmaraş, Turkey earthquake sequence in the East Anatolian Fault Zone, *Seismica*, *2*(3), doi:10.26443/seismica.v2i3.502.

313 Ben-Zion, Y., M. Eneva, and Y. Liu (2003), Large earthquake cycles and intermittent criticality
314 on heterogeneous faults due to evolving stress and seismicity, *J. Geophys. Res.*, *108*(B6), doi:
315 https://doi.org/10.1029/2002JB002121.

316 Benioff, H. (1935), A linear strain seismograph*, *Bull. Seismo. Soc. Am.*, *25*(4), 283–309, doi:
317 10.1785/BSSA0250040283.

318 Brodsky, E. E., V. Karakostas, and H. Kanamori (2000), A new observation of dynamically
319 triggered regional seismicity: Earthquakes in Greece following the August 1999 Izmit, Turkey
320 earthquake, *Geophys. Res. Lett.*, *27*(17), 2741–2744, doi:10.1029/2000GL011534.

321 Brune, J. N. (1970), Tectonic stress and the spectra of seismic shear waves from earthquakes, *J.*
322 *Geophys. Res.*, *75*(26), 4997–5009, doi:10.1029/JB075i026p04997.

323 Chen, T., and N. Lapusta (2009), Scaling of small repeating earthquakes explained by interaction
324 of seismic and aseismic slip in a rate and state fault model, *J. Geophys. Res*, *114*, 1311, doi:
325 10.1029/2008JB005749.

326 Dieterich, J. H. (1972), Time-dependent friction in rocks, *J. Geophys. Res. (1896-1977)*, *77*(20),
327 3690–3697, doi:https://doi.org/10.1029/JB077i020p03690.

328 Fitch, T. J. (1975), Compressional velocity in source regions of deep earthquakes: An appli-
329 cation of the master earthquake technique, *Earth Planet. Sci. Lett.*, *26*(2), 156–166, doi:
330 https://doi.org/10.1016/0012-821X(75)90083-7.

331 Gibbons, S. J., and F. Ringdal (2006), The detection of low magnitude seismic events us-
332 ing array-based waveform correlation, *Geophys J. Int.*, *165*(1), 149–166, doi:10.1111/j.1365-
333 246X.2006.02865.x.

334 Gitterman, Y., V. Pinsky, and A. Shapira (2003), Improvements in Monitoring the CTBT in the
335 Middle East by the Israel Seismic Network, *Tech. Rep. October*, Perpared for: Defense Threat

Reduction Agency, USA.

Gomberg, J., and D. Agnew (1996), The accuracy of seismic estimates of dynamic strains: An evaluation using strainmeter and seismometer data from Piñon Flat Observatory, California, *Bull. Seismo. Soc. Am.*, *86*(1 SUPPL. A), 212–220.

Gomberg, J., and P. Johnson (2005), Dynamic triggering of earthquakes, *Nature*, *437*(7060), 830–830, doi:10.1038/437830a.

Gomberg, J., P. A. Reasenberg, P. Bodin, and R. A. Harris (2001), Earthquake triggering by seismic waves following the Landers and Hector Mine earthquakes, *Nature*, *411*(6836), 462–466, doi:10.1038/35078053.

Heimisson, E. R. (2019), Constitutive Law for Earthquake Production Based on Rate-and-State Friction: Theory and Application of Interacting Sources, *J. Geophys. Res.*, *124*(2), 1802–1821, doi:10.1029/2018JB016823.

Helmstetter, A., G. Ouillon, and D. Sornette (2003), Are aftershocks of large Californian earthquakes diffusing?, *J. Geophys. Res.*, *108*(B10), doi:https://doi.org/10.1029/2003JB002503.

Hill, D. P., P. A. Reasenberg, A. Michael, W. J. Arabaz, G. Beroza, D. Brumbaugh, J. N. Brune, R. Castro, S. Davis, D. DePolo, W. L. Ellsworth, J. Gomberg, S. Harmsen, L. House, S. M. Jackson, M. J. S. Johnston, L. Jones, R. Keller, S. Malone, L. Munguia, S. Nava, J. C. Pechmann, A. Sanford, R. W. Simpson, R. B. Smith, M. Stark, M. Stickney, A. Vidal, S. Walter, V. Wong, and J. Zollweg (1993), Seismicity Remotely Triggered by the Magnitude 7.3 Landers, California, Earthquake, *Science*, *260*(5114), 1617–1623, doi:10.1126/science.260.5114.1617.

Inbal, A., J.-P. Ampuero, and J.-P. Avouac (2017), Locally and remotely triggered aseismic slip on the central San Jacinto Fault near Anza, CA, from joint inversion of seismicity and strainmeter data, *J. Geophys. Res.*, *122*(4), doi:10.1002/2016JB013499.

359 Kilb, D., J. Gomberg, and P. Bodin (2000), Triggering of earthquake aftershocks by dynamic
360 stresses, *Nature*, *408*(6812), 570–574, doi:10.1038/35046046.

361 King, G. C. P., R. S. Stein, and J. Lin (1994), Static Stress Changes and the Triggering of
362 Earthquakes, *84*(3), 935–953.

363 Lior, I., and A. Ziv (2020), Generic Source Parameter Determination and Ground-Motion
364 Prediction for Earthquake Early Warning, *Bull. Seis. Soc. Am.*, *110*(1), 346–356, doi:
365 10.1785/0120190140.

366 Marone, C., J. E. Vidale, and W. L. Ellsworth (1995), Fault healing inferred from time dependent
367 variations in source properties of repeating earthquakes, *Geophys. Res. Lett.*, *22*(22), 3095–
368 3098, doi:https://doi.org/10.1029/95GL03076.

369 Marsan, D. (2005), The role of small earthquakes in redistributing crustal elastic stress, *Geophys.*
370 *J. Int.*, *163*(1), 141–151, doi:10.1111/j.1365-246X.2005.02700.x.

371 Mikumo, T., and K. Aki (1964), Determination of local phase velocity by intercomparison of
372 seismograms from strain and pendulum instruments, *J. Geophys. Res.*, *69*(4), 721–731, doi:
373 https://doi.org/10.1029/JZ069i004p00721.

374 Nadeau, R., M. Antolik, P. A. Johnson, W. Foxall, and T. V. McEvilly (1994), Seismological
375 studies at Parkfield III: Microearthquake clusters in the study of fault-zone dynamics, *Bull.*
376 *Seismo. Soc. Am.*, *84*(2), 247–263, doi:10.1785/BSSA0840020247.

377 Omori, F. (1894), On the Aftershocks of Earthquakestle, *Journal of the College of Science*, *7*,
378 111–120.

379 Schaff, D. P., G. C. Beroza, and B. E. Shaw (1998), Postseismic response of repeating aftershocks,
380 *Geophys. Res. Lett.*, *25*(24), 4549–4552, doi:10.1029/1998GL900192.

Scholz, C., P. Molnar, and T. Johnson (1972), Detailed studies of frictional sliding of granite and implications for the earthquake mechanism, *J. Geophys. Res.*, *77*(32), 6392–6406, doi: https://doi.org/10.1029/JB077i032p06392.

Scholz, C. H., and J. T. Engelder (1976), The role of asperity indentation and ploughing in rock friction — I: Asperity creep and stick-slip, *Int. J. Rock Mech. Min.*, *13*(5), 149–154, doi:https://doi.org/10.1016/0148-9062(76)90819-6.

Segall, P. (2010), *Earthquake and Volcano Deformation*, Princeton University Press.

Sharon, M., A. Sagy, I. Kurzon, S. Marco, and M. Rosensaft (2020), Assessment of seismic sources and capable faults through hierarchic tectonic criteria: implications for seismic hazard in the Levant, *Natural Hazards and Earth System Sciences*, *20*(1), 125–148, doi:10.5194/nhess-20-125-2020.

Vidale, J. E., W. L. EllIsworth, A. Cole, and C. Marone (1994), Variations in rupture process with recurrence interval in a repeated small earthquake, *Nature*, *368*(6472), 624–626, doi: 10.1038/368624a0.

Ziv, A. (2006a), On the role of multiple interactions in remote aftershock triggering: The Landers and the Hector Mine case studies, *Bull. Seismo. Soc. Am.*, *96*(1), 80–89, doi: 10.1785/0120050029.

Ziv, A. (2006b), What controls the spatial distribution of remote aftershocks?, *Bull. Seismo. Soc. Am.*, *96*(6), 2231–2241, doi:10.1785/0120060087.

Ziv, A., and J. Schmittbuhl (2003), The seismic cycle and the difference between foreshocks and aftershocks in a mechanical fault model, *Geophys. Res. Lett.*, *30*(24), doi: https://doi.org/10.1029/2003GL018665.